

LoMu: Enable Long-Range Multi-Target Backscatter Sensing for Low-Cost Tags

Yihao Liu, Jinyan Jiang and Jiliang Wang

School of Software

Tsinghua University, P.R. China

{liu-yh23,jiangjy23}@mails.tsinghua.edu.cn, jiliangwang@tsinghua.edu.cn

Abstract—Backscatter sensing has shown great potential in the Internet of Things (IoT) and has attracted substantial research interest. We present LoMu, the first long-range multi-target backscatter sensing system for low-cost tags under ambient LoRa. LoMu analyzes the received low-SNR backscatter signals from different tags and calculates their phases to derive the motion information. The design of LoMu faces practical challenges including near-far interference between multiple tags, phase offsets induced by unsynchronized transceivers, and phase errors due to frequency drift in low-cost tags. We propose a conjugate-based energy concentration method to extract high-quality signals and a Hamming-window-based method to alleviate the near-far problem. We then leverage the relationship between the excitation signal and backscatter signals to synchronize TX and RX. Finally, we combine the double sidebands of backscatter signals to cancel the tag frequency drift. We implement LoMu and conduct extensive experiments to evaluate its performance. The results demonstrate that LoMu can accurately sense 35 tags at the same time. The average frequency sensing error is 0.7% at 400m, which is $4\times$ distance of the state-of-the-art.

Index Terms—LoRa, Backscatter, Long-Range Sensing, Multi-Target Sensing

I. INTRODUCTION

Wireless sensing, which acquires information about objects through wireless signals, has attracted extensive attention in the last few years. A range of wireless technologies traditionally used for communication are now being exploited for sensing. These technologies include RFID [1]–[7], WiFi [8]–[13], UWB [14]–[17], FMCW radar [18]–[20], and visible light [21]–[24], with typical applications spanning object localization [8], [9], [17], [24], vibration detection [1]–[3], respiration monitoring [11]–[16], [18] and gesture recognition [10], [13], [22], [24].

Backscatter sensing systems have brought small form factors and low power consumption to wireless sensing. Notably, LoRa backscatter sensing systems, as explored in the works [25], [26], demonstrate promising capabilities in extending the sensing range. For example, Palantir [25] can accurately detect the vibration of a single target within a range of 100m. Despite these advancements, practical long-range sensing for multiple low-cost tags remains challenging due to specific issues: (1) Unsynchronized transceivers: The presence of offsets, such as carrier frequency offset (CFO), between the transmitter (TX) and receiver (RX) leads to significant sensing errors. Marvel [26] requires a common external reference clock for TX and RX synchronization. On

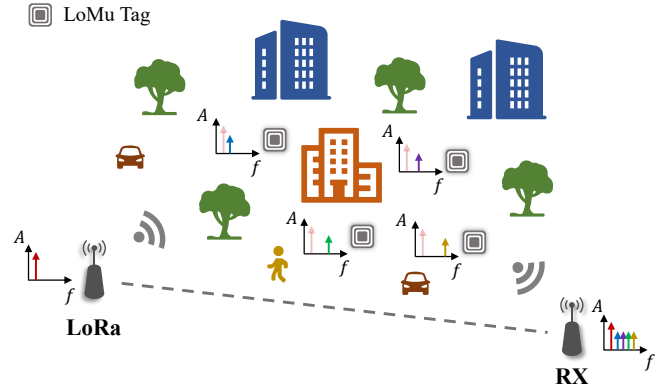


Fig. 1: The principle of LoMu.

the other hand, Palantir employs a curve-fitting method to address these offsets. However, this method is susceptible to environmental noise, impacting the accuracy of sensing results. (2) Frequency drift in low-cost tags. The distortion of backscatter signals due to frequency drift in low-cost tags introduces sensing errors. While Marvel assumes a constant tag frequency over time, Palantir utilizes a clustering method to extract phases of backscatter signals. Unfortunately, the accuracy of sensing decreases significantly in the presence of tag frequency drift. The attainment of practical long-range multi-target sensing holds promise for numerous applications, including but not limited to multi-person respiration sensing, large-area building vibration monitoring, etc.

In this work, we present *LoMu*, the first **Long-range Multi-target** backscatter sensing system for low-cost tags under ambient LoRa. As shown in Fig. 1, a LoMu tag requires only a frequency shift of ambient LoRa signals. The LoMu receiver adeptly extracts low SNR backscatter signals from multiple tags and computes the corresponding signal characteristics for sensing. Crucially, LoMu seamlessly integrates with commodity-off-the-shelf (COTS) LoRa devices and is capable of handling low-cost tags with frequency drift. To put this into practice, we shall address the following challenges:

(1) *How to enhance the SNR of sensing signals?* Palantir [25] utilizes time samples for calculating signal phases, imposing a high signal-to-noise ratio (SNR) requirement that limits the sensing range (e.g., only 100m). To enhance energy concentration in low-SNR scenarios, we observe that the

dechirped LoRa signals often split into two parts, leading us to propose a conjugate demodulation schema. Moreover, in long-range backscatter systems, the sensing accuracy may be compromised by the well-known near-far problem. This problem arises when the side lobes of a strong signal mask the main lobe of a weaker one after the Fast Fourier Transform (FFT). In response, we introduce a Hamming-window-based method to alleviate the near-far problem.

(2) *How to synchronize TX and RX?* In cases where Tx and Rx are not synchronized, random phase offsets emerge in the received signals. These additional offsets are mixed with phase changes induced by target movements, rendering it impossible to extract target information. Previous works [26]–[29] exploit an external reference clock to synchronize Tx and Rx. However, this approach does not apply to LoRa sensing systems when Tx and Rx are separated by tens of meters. Zhang et al. [30] employ two antennas to address this problem. Palantir [25] uses a curve-fitting method, although this approach can be sensitive to low SNR. In this work, we show similar offsets experienced by both the excitation signal and target reflection signals. This similarity serves as a foundation for removing offsets between unsynchronized transceivers.

(3) *How to cancel frequency drift in low-cost tags?* It is impractical to expect backscatter tags to maintain stable frequencies, as they are typically equipped with imprecise oscillators to reduce costs. Therefore, their frequencies drift over time, resulting in phase errors in target reflection signals. μLocate [27] attempts to measure tag frequency drift and compensate for phase errors. This method, however, may not offer the precision required for sensing applications. LocRa [31] performs phase interpolation between two measurements of the same channel to correct phase errors. Nevertheless, this method may not be suitable for our work as we do not have two identical channels. In this work, we rely on the fundamental characteristic of tag modulation. By capitalizing on this characteristic, we successfully address errors arising from tag frequency drift. This method is simple yet robust and is effective regardless of the extent of tag frequency drift.

Our contributions can be summarized as follows:

- We present LoMu, a pioneering long-range multi-target backscatter sensing system designed for ambient LoRa. LoMu is compatible with both low-cost tags and COTS LoRa devices. Remarkably, it operates without the need for cable-based or multi-antennae-based TX-RX synchronization. These features underscore the simplicity and capability of LoMu.
- We introduce the sensing model for long-range multi-target backscatter sensing systems, offering a comparison analysis with those from other works such as Palantir [25]. Additionally, we shed light on the key challenges encountered in practice, involving the near-far problem, offsets caused by unsynchronized TX and RX, and frequency drift in low-cost tags. To address these challenges, we propose corresponding methods and provide thorough verification

of their effectiveness.

- We have implemented LoMu and carried out extensive experiments to evaluate its performance. The results underscored the remarkable capabilities of LoMu, demonstrating its ability to simultaneously sense at least 35 tags. The sensing range of LoMu reached 400m, surpassing the state-of-the-art by $4\times$. Even in this considerable distance, the average sensing error remained low at 0.7%.

RoadMap. The structure of this paper is as follows. In Sec. II, we introduce the sensing model and discuss key challenges encountered in practice. In Sec. III, we offer an in-depth description of our system design, elucidating the effective methods employed. In Sec. IV, we showcase experimental results and a case study. Sec. V provides a survey of related works, and we discuss and conclude our work in Sec. VI and Sec. VII.

II. SENSING MODEL & CHALLENGES

In this section, we begin by introducing the principles of LoRa and backscatter. Subsequently, we present a multi-target sensing model for the excitation signal and backscatter signals. Additionally, we conduct a comparative analysis with sensing models from other works. Finally, we highlight the practical challenges associated with the proposed sensing model.

A. LoRa Backscatter

1) *LoRa:* LoRa adopts a chirp spreading spectrum (CSS) mechanism for modulation, facilitating a long communication range. In LoRa, data is modulated using chirps, whose frequency changes linearly over time. The LoRa transmitter encodes different data by selecting the initial frequency of the chirp. Given the initial frequency f_0 and frequency change rate k , a LoRa chirp can be represented as:

$$S(t) = e^{j2\pi(f_0 t + \frac{1}{2} k t^2)} \quad (1)$$

where $k = \frac{BW}{T}$. BW and T are the bandwidth and length of the chirp, respectively. LoRa has an additional parameter SF to characterize the relationship between BW and T :

$$2^{SF} = BW \cdot T \quad (2)$$

As shown in Fig. 2, the base chirp is a chirp with $f_0 = -\frac{BW}{2}$, while the data chirp is a chirp with a specific initial frequency f_0 corresponding to its encoded data. For different data chirps, there are 2^{SF} choices of f_0 .

For demodulation, the receiver multiplies the incoming chirp with a down chirp, whose frequency decreases from $\frac{BW}{2}$ to $-\frac{BW}{2}$. The down chirp is conjugated to the base chirp and can be represented as:

$$S_{down}(t) = e^{j2\pi(\frac{BW}{2}t - \frac{1}{2} k t^2)} \quad (3)$$

After multiplication, namely *dechirp* operation, the received signal is converted into a sinusoid:

$$S(t) \cdot S_{down}(t) = e^{j2\pi(f_0 + \frac{BW}{2})t} \quad (4)$$

The frequency of the sinusoid is $f_0 + \frac{BW}{2}$. To demodulate data, we apply FFT and search for peaks.

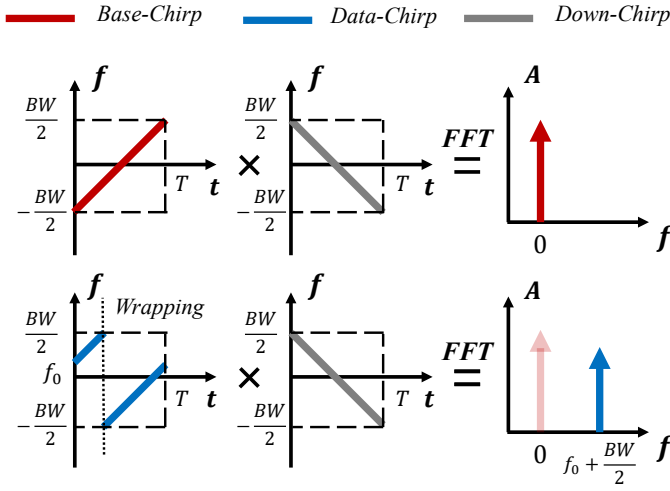


Fig. 2: LoRa modulation and demodulation.

2) *Backscatter*: A LoMu tag is an FSK-modulated tag, which switches between two impedances to generate a square wave for frequency shifting. Given the frequency of the RF switch f_{tag} and the incoming signal $s_i(t)$, the backscatter signal can be represented as:

$$s_b(t) = s_i(t) \cdot e^{(2\pi f_{tag}t + \psi_{tag})} \quad (5)$$

where ψ_{tag} is the initial phase of the generated wave. It is worth mentioning that different LoMu tags have different shifting frequencies.

B. LoMu Sensing Model

Without loss of generality, we assume the signal propagation scenario is as shown in Fig. 3. The baseband signal is an arbitrary LoRa chirp (i.e., $s_0(t) = S(t)$).

1) *Excitation signal*: The signal sent by the transmitter is an upconversion of the baseband signal:

$$s_1(t) = s_0(t) \cdot e^{j2\pi f_c t} \cdot e^{j\varphi_{TX}} \quad (6)$$

where f_c and φ_{TX} are the frequency and initial phase of the transmitter carrier, respectively. After time τ , the signal propagates to the receiver and is downconverted:

$$\begin{aligned} s_2(t) &= \alpha \cdot s_1(t - \tau) \cdot e^{-j2\pi f_c t} \cdot e^{-j\varphi_{RX}} \\ &= \alpha \cdot s_0(t - \tau) \cdot e^{-j2\pi f_c \tau} \cdot e^{j(\varphi_{TX} - \varphi_{RX})} \end{aligned} \quad (7)$$

where φ_{RX} is the initial phase of the receiver carrier. The receiver multiplies the received signal with a down chirp, applies FFT, and extracts the phase of the peak at the excitation frequency bin:

$$\theta_E = -2\pi f_c \tau + \varphi_{TX} - \varphi_{RX} \quad (8)$$

2) *Backscatter signals*: After time τ_1 , the tag also picks up the signal sent by the transmitter and shifts its frequency when reflected:

$$\begin{aligned} s_3(t) &= \alpha_1 \cdot s_1(t - \tau_1) \cdot e^{j(2\pi f_{tag}t + \psi_{tag})} \\ &= \alpha_1 \cdot s_0(t - \tau_1) \cdot e^{j2\pi f_c(t - \tau_1)} \cdot e^{\varphi_{TX}} \\ &\quad \cdot e^{j(2\pi f_{tag}t + \psi_{tag})} \end{aligned} \quad (9)$$

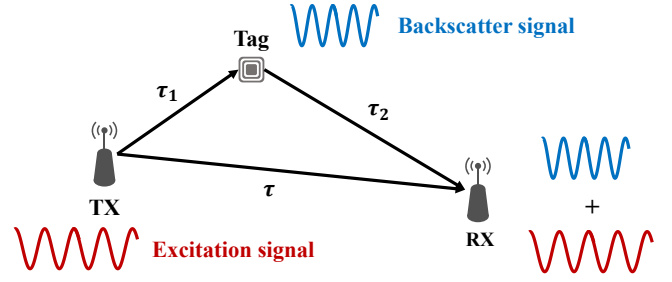


Fig. 3: LoMu sensing model.

The backscatter signal propagates to the receiver after time τ_2 and is downconverted:

$$\begin{aligned} s_4(t) &= \alpha_2 \cdot s_3(t - \tau_2) \cdot e^{-j2\pi f_c t} \cdot e^{-j\varphi_{RX}} \\ &= \alpha_1 \alpha_2 \cdot s_0(t - \tau_1 - \tau_2) \cdot e^{-j2\pi f_c(\tau_1 + \tau_2)} \\ &\quad \cdot e^{j(\varphi_{TX} - \varphi_{RX})} \cdot e^{j(2\pi f_{tag}(t - \tau_2) + \psi_{tag})} \end{aligned} \quad (10)$$

After applying the same operations as when extracting θ_E , we obtain the phase of the backscatter signal at the backscatter frequency bin:

$$\begin{aligned} \theta_B &= -2\pi f_c(\tau_1 + \tau_2) + \varphi_{TX} - \varphi_{RX} \\ &\quad + 2\pi f_{tag}(\tau - \tau_2) + \psi_{tag} \end{aligned} \quad (11)$$

Here, we neglect the negligible baseband phase $s_0(\tau - \tau_1 - \tau_2)$. For scenarios involving multiple tags, we acquire the phases θ_{B_i} corresponding to different tags i at FFT bins f_{tag_i} .

In Eq. (11), the term $-2\pi f_c(\tau_1 + \tau_2)$ is our target. As shown in Fig. 3, this term corresponds to the total distance from the tag to both TX and RX. By calculating the changes in this term, we can effectively sense the movement of the tag.

C. Comparison with Previous Sensing Models

To illustrate the distinction between our sensing model and those in previous works [3], [25], [30], we provide a simple yet essential explanation. Here, we temporarily set aside some details, as they do not impact the rationale of the sensing models.

Suppose there are some static paths, including the line-of-sight path and reflection path from stationary objects, and dynamic paths, which are reflection paths from multiple moving targets [3], [25], [30]. When targets are in motion, the dynamic paths change, while the static paths remain stable. In previous sensing models, the received signals can be represented as:

$$r_1(t) = \sum_{s=1}^S \alpha_s e^{j\varphi_s} + \sum_{d=1}^D \alpha_d e^{j\varphi_d} \quad (12)$$

where s and d denote the s th static path and d th dynamic path, respectively. In the same scenario, the received signals in our sensing model can be represented as:

$$r_1(t) = \sum_{s=1}^S \alpha_s e^{j\varphi_s} + \sum_{d=1}^D \alpha_d e^{j\varphi_d} \cdot e^{j2\pi f_d t} \quad (13)$$

Both sensing models rely on the variations in φ_d to sense the targets. However, when there are multiple dynamic paths (i.e., $D > 1$), the previous sensing models encounter challenges as the signals overlap at the receiver. In contrast, our sensing model excels in distinguishing different targets, leveraging the orthogonality of their reflection signals (i.e., different tags have different frequencies f_d).

D. Challenges in Practice

Other terms in Eq. (11) in addition to the one of interest (i.e., $-2\pi f_c(\tau_1 + \tau_2)$) pose practical challenges, including:

1) *Interference from near-far tags:* While distinguishing backscatter signals from tags with different shifting frequencies is achievable, the signals may face a near-far problem. Spectrum leakage causes each backscatter signal to generate lobes in the frequency domain after FFT. The near-far problem occurs when the main lobe of weak backscatter signals is masked by the side lobes of stronger ones, resulting in signal loss and potential sensing failure.

2) *Offsets induced by the unsynchronized transceivers:* The term $\varphi_{TX} - \varphi_{RX}$ in Eq. (11) varies randomly when TX and RX are not synchronized. With a carrier frequency offset (CFO) denoted as $f_{CFO}(t)$, this term can be expressed as:

$$\varphi_{CFO} = \varphi_{TX} - \varphi_{RX} = \int_0^t 2\pi f_{CFO}(t)dt + \varphi_0 \quad (14)$$

where φ_0 represents the difference between the initial phases of TX and RX carriers at time 0. This offset is significant. For example, with a $f_{CFO} = 1\text{Hz}$, the phase offset will accumulate to 2π after 1s, equivalent to 70cm when the carrier frequency is 433MHz. Compared to the millimeter-level movement of tags, this offset is orders of magnitude higher. Apart from this, the sample time offset (STO) and the sample frequency offset (SFO) also introduce errors.

3) *Errors caused by tag frequency drift:* Although we can neglect the term $2\pi f_{tag}(\tau - \tau_2)$ in Eq. (11) because f_{tag} is orders of magnitude lower than f_c , it becomes challenging to cancel the term ψ_{tag} when the shifting frequency of tag drifts. This drift incurs phase errors represented as:

$$\epsilon = \int_0^t 2\pi (f_{tag}(t) - f_{tag}(0)) dt \quad (15)$$

These errors change over time and are more significant than the offsets caused by unsynchronized TX and RX, especially considering that low-cost tags are typically equipped with less stable oscillators. Removing these errors is hard since they are blended with phase changes induced by tag movement.

III. LOMU SYSTEM DESIGN

In this section, we first provide an overall design of LoMu. Subsequently, we delve into the detailed introduction of the main modules and discuss how to address practical challenges.

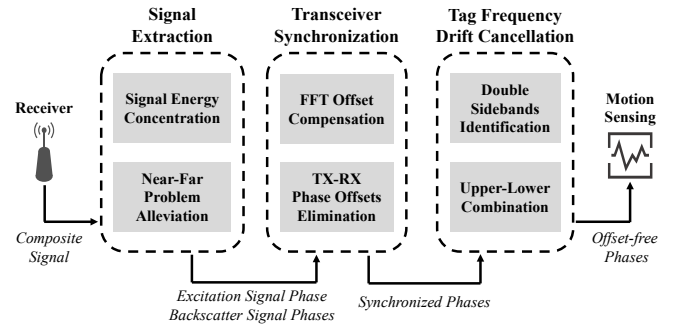


Fig. 4: The main workflow and components of LoMu.

A. Design Overview

The workflow of LoMu is illustrated in Fig. 4, which consists of four modules:

Signal Extraction. This module aims to extract high-SNR signals for accurate sensing. We propose a conjugate demodulation schema on top of the standard LoRa demodulation schema to concentrate all the energy of received signals. Additionally, we propose a Hamming-window-based method to mitigate the near-far problem. Finally, this module performs an FFT to extract the excitation signal phase and backscatter signal phases.

Transceiver Synchronization. This module shines a light on removing offsets caused by unsynchronized TX and RX. Initially, we compensate for the FFT-induced offsets. Then, we utilize the relationship between the excitation signal and backscatter signals to address other offsets such as CFO, STO, and SFO.

Tag Frequency Drift Cancellation. This module aims to eliminate phase errors caused by frequency drift in tags. We tackle this challenge by first identifying the double sidebands of a backscatter signal and then combining both sidebands.

Motion Sensing. This module leverages phase changes to extract motion information.

B. Conjugate-based Energy Concentration

In Sec. II-A1, we introduced the standard demodulation schema of LoRa: the receiver multiplies the incoming chirp with the down chirp and then applies FFT to obtain the initial frequency. However, due to the wrapping of frequency in the chirp, the received signal is converted into two discontinuous sinusoids with frequencies $f_0 + \frac{BW}{2}$ and $f_0 - \frac{BW}{2}$, respectively. If the sampling frequency of the receiver equals the bandwidth of the chirp, the two sinusoids will alias together and produce the same peak after FFT. To sample the signal from multiple tags in LoMu, however, the sampling frequency of the receiver should be larger than the bandwidth of the chirp. As shown in Fig. 6a, this splits the energy into two parts, leading to energy loss.

To maximize the SNR of signals, we propose a conjugate demodulation schema on top of the standard LoRa demodulation schema. In this schema, we multiply the incoming chirp by the conjugate chirp after the standard LoRa demodulation.

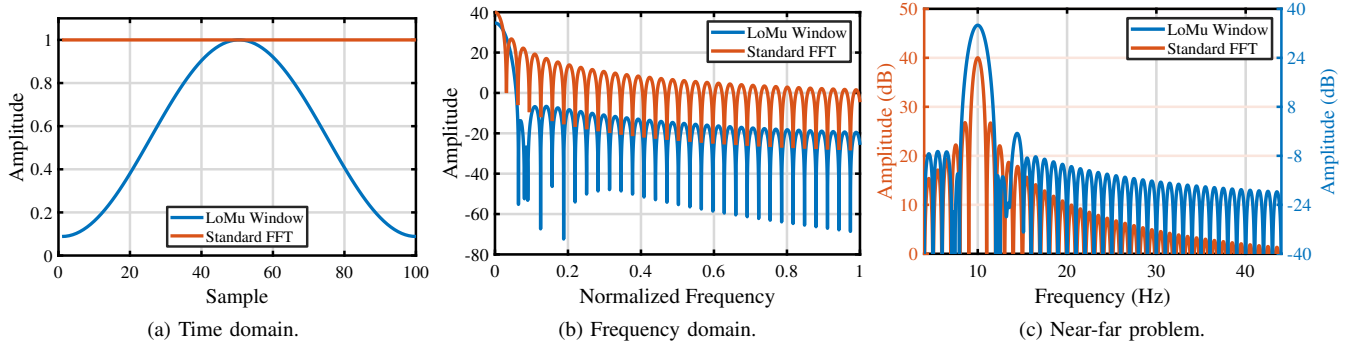


Fig. 5: The comparison between LoMu window and standard FFT.

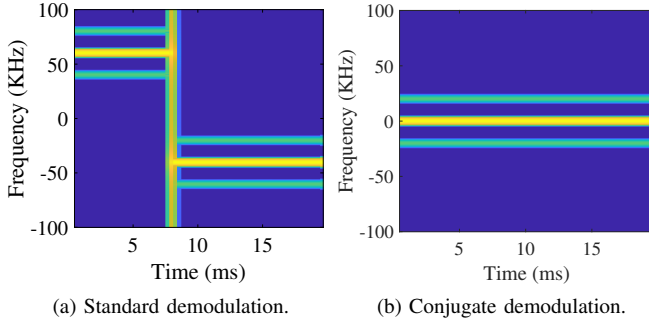


Fig. 6: The comparison between standard demodulation and conjugate-based energy concentration.

We decode the initial frequency of each chirp using the excitation signal and then generate the conjugate version of each chirp as:

$$S^*(t) = e^{-j2\pi(f_0 t + \frac{1}{2} k t^2)} \quad (16)$$

Following these operations, we convert the excitation signal and backscatter signals into continuous sinusoids. As shown in Fig. 6b, the energy of each sinusoid is concentrated in the corresponding FFT bin.

C. Near-far Problem Alleviation

According to the principle of FFT, the main-lobe width of a sine wave with a time length T is given by $\frac{2}{T}$. For instance, when the time window is 8ms, the main-lobe width is 250Hz. In practical scenarios, we can design the shifting frequency between two tags to be greater than 250Hz. However, the near-far problem introduces challenges, where the main lobe of a weak backscatter signal might be disturbed by the side lobes of strong signals.

To mitigate the impact of side lobes and address the near-far problem, we employ a window function, a classic technique discussed in the literature [32]. A window function is designed to weight samples in the time domain, influencing results in the frequency domain. In our case, we utilize a Hamming window, which smoothly reduces the amplitude of a signal from the center to both edges. To enhance the near-far problem

alleviation, we incorporate a DC term and the third harmonic of the cosine function into the Hamming window as introduced in the work [33]. This results in a main-lobe width less than or equal to that of the Hamming window and provides about 2-4.5dB smaller peak side-lobe amplitude. The time and frequency domains of the LoMu window, compared with the standard FFT, are illustrated in Fig. 5a and Fig. 5b.

Upon combining the customized window function, we proceed to extract the excitation phase at the excitation frequency bin and the backscatter phases at the backscatter frequency bins.

Experiment: We verified the effectiveness of our method in a near-far scenario involving two tag signals, where one signal was $10000\times$ (40 dB) stronger than the other. Fig. 5c shows the result that our method successfully extracted the weaker signal by suppressing the side lobes of the stronger one.

D. TX-RX Phase Offset Elimination

The combined impact of CFO, STO, and SFO on the excitation signal and backscatter signals can be expressed as follows:

$$\varphi_E = 2\pi f_{CFO}m(t + t_{STO}) + s_0(m(t + t_{STO})) - s_0(t) \quad (17)$$

$$\varphi_B = 2\pi f_{CFO}m(t + t_{STO} + \tau_\Delta) + s_0(m(t + t_{STO} + \tau_\Delta)) - s_0(t) + 2\pi f_{tag}mt_{STO} \quad (18)$$

where τ_Δ is a notation of $\tau - \tau_1 - \tau_2$, and f_{CFO}, t_{STO}, m are the impact of CFO, STO, and SFO, respectively. In practice, we measure the phases of the excitation signal and backscatter signals as $\hat{\theta}_B = \theta_B + \varphi_B$ and $\hat{\theta}_E = \theta_E + \varphi_E$. The difference between $\hat{\theta}_B$ and $\hat{\theta}_E$ is then calculated as:

$$\begin{aligned} \hat{\theta}_B - \hat{\theta}_E &= \theta_B - \theta_E + \varphi_B - \varphi_E \\ &\approx \theta_B - \theta_E + 2\pi f_{tag}mt_{STO} \\ &= 2\pi f_c(\tau - (\tau_1 + \tau_2)) \\ &\quad + 2\pi f_{tag}(\tau - \tau_2) \\ &\quad + \psi_{tag} \\ &\quad + 2\pi f_{tag}mt_{STO} \end{aligned} \quad (19)$$

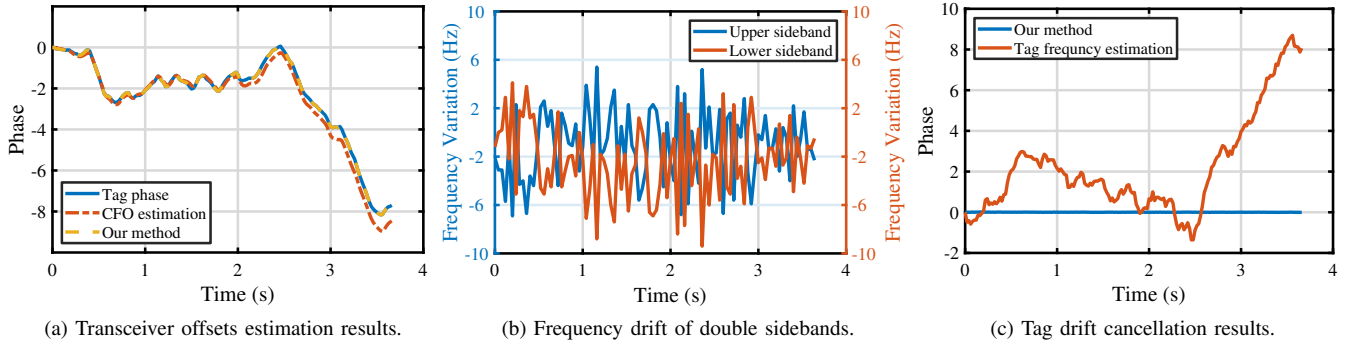


Fig. 7: The offsets and errors induced by unsynchronized transceivers and tag frequency drift.

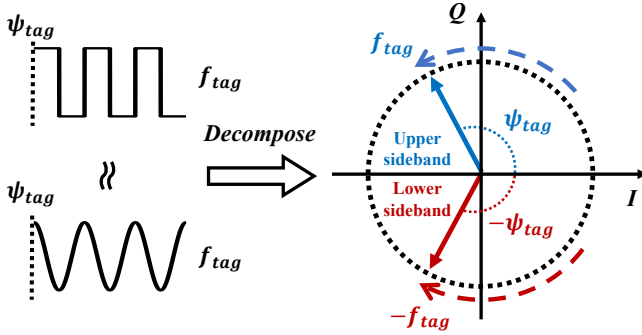


Fig. 8: Decomposition of a generated square wave.

where:

$$\begin{aligned} \varphi_B - \varphi_E &= 2\pi(f_0 + f_{CFO})m\tau_\Delta \\ &\quad + \pi km^2\tau_\Delta(2t_{STO} + \tau_\Delta) \\ &\quad + 2\pi f_{tag}mt_{STO} \\ &\approx 2\pi f_{tag}mt_{STO} \end{aligned} \quad (20)$$

In Eq. (20), f_{CFO} and f_0 are at most hundreds of kilohertz and τ_Δ is a few nanoseconds. Thus, the first few terms in Eq. (20) are approximately equal to zero. By calculating the phase difference between the excitation signal and backscatter signals, we effectively eliminate the impact of unsynchronized TX and RX.

Experiment: We compared our method with a CFO-based estimation method mentioned in P²LoRa [34]. P²LoRa exploits the up-chirp and down-chirp in the LoRa preamble to estimate CFO, which can be integrated to calculate the phase offset. Fig. 7a shows the comparison of the phase offset estimation results. We can observe that our elimination method achieved a maximum estimation error of 0.013, while the CFO integration method had an error of up to 5.925 due to severe numerical integration errors.

E. Tag Frequency Drift Cancellation

Due to the frequency drift in tags, extracting the first term in Eq. (19) (i.e., $2\pi f_c(\tau - (\tau_1 + \tau_2))$) becomes challenging. To address this problem, our key observation is that there are two opposite sidebands of a backscatter signal. As shown

in Fig. 8, an RF switch generates a square wave, which is further decomposed into two sinusoids and corresponding harmonics in the complex domain. Therefore, in addition to the backscatter signal described in Sec. II-A2, there exists another backscatter signal:

$$s_b^{down}(t) = s_i(t) \cdot e^{-(2\pi f_{tag}t + \psi_{tag})} \quad (21)$$

These two backscatter signals represent the upper and lower sidebands of a backscatter signal. By substituting f_{tag} with $-f_{tag}$ and ψ_{tag} with $-\psi_{tag}$ in Eq. (19) (i.e., $\hat{\theta}_B^{up} - \hat{\theta}_E$), we obtain the phases of the lower sideband signals:

$$\begin{aligned} \hat{\theta}_B^{down} - \hat{\theta}_E &= 2\pi f_c(\tau - (\tau_1 + \tau_2)) \\ &\quad - 2\pi f_{tag}(t - \tau - \tau_2) \\ &\quad - \psi_{tag} \\ &\quad - 2\pi f_{tag}mt_{STO} \end{aligned} \quad (22)$$

Indeed, the essential characteristic of tag modulation reveals that if the upper sideband signal encounters an error of ϵ_{tag} , the lower sideband signal experiences an error of $-\epsilon_{tag}$. We can combine the phases of the two sidebands to address tag frequency drift:

$$\begin{aligned} \theta_{tag} &= \frac{\hat{\theta}_B^{up} - \hat{\theta}_E}{2} + \frac{\hat{\theta}_B^{down} - \hat{\theta}_E}{2} \\ &= 2\pi f_c(\tau - (\tau_1 + \tau_2)) \end{aligned} \quad (23)$$

Experiment: To showcase the effectiveness of our method, we carried out an experiment. Initially, we measured the double sideband frequency of a tag as depicted in Fig. 7b, which reveals opposite frequency variations in the two sidebands. Subsequently, we integrated the measured frequency into phase errors and compared the compensation performance with our method. Fig. 7c shows the results that our method completely removed the phase errors, while the estimated phase errors quickly escalated to 3.

F. Motion Sensing

We can translate phase changes $\Delta\theta_{tag}$ into distance changes. To enhance sensing results, additional filtering techniques can be employed. For example, a Kalman filter can mitigate thermal noise during sensing [35]. A band-pass filter can

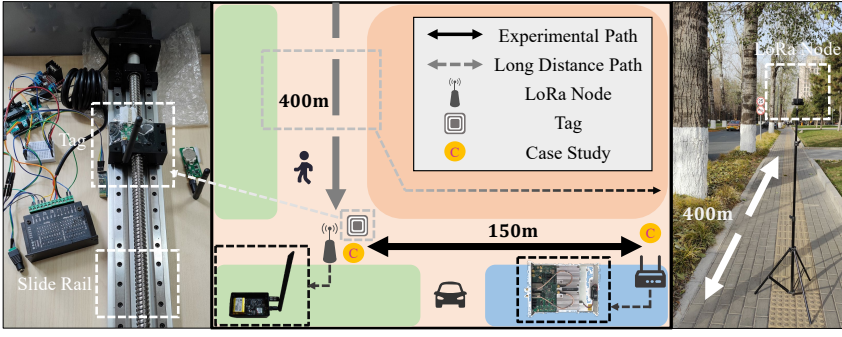


Fig. 9: Experimental hardware and field.

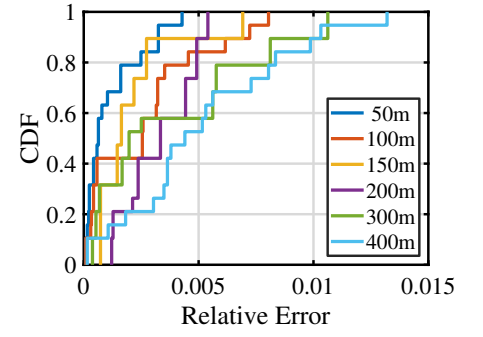


Fig. 10: Impact of TX-RX distance.

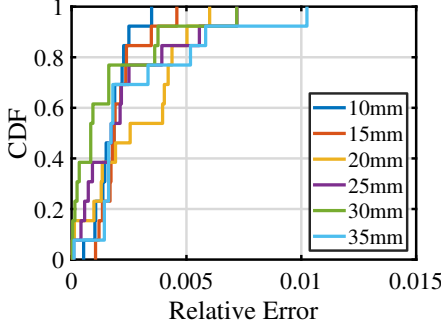


Fig. 11: Impact of motion amplitude.

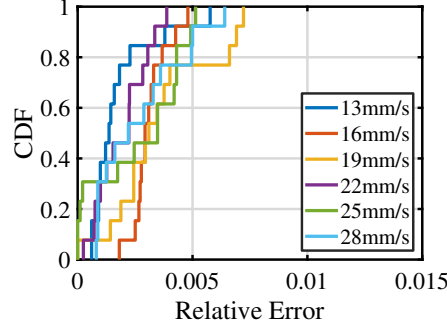


Fig. 12: Impact of motion speed.

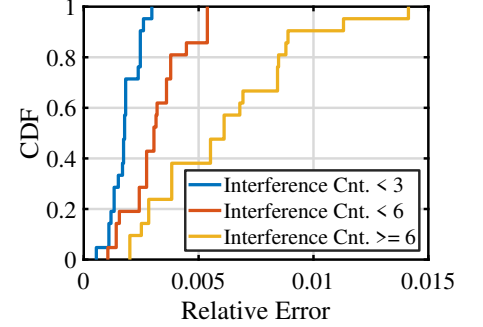


Fig. 13: Impact of interference.

be used to enhance vibration sensing results, and a high-pass filter may be effective when the transmitter is moving [25]. Finally, we perform an FFT on the distance changes to acquire tag motion frequency. It is worth mentioning that changes in signal amplitude also contribute to improving the accuracy of the detected frequency.

IV. EVALUATION

In this section, we present experimental results to showcase the performance of LoMu. Section IV-A provides details about the hardware and experimental setup. Section IV-B evaluates LoMu under various settings using a controllable slide rail. Finally, in Section IV-C, we present a case study illustrating the feasibility of LoMu for multi-target respiration monitoring.

A. Experimental Setup

In our experiments, we used a COTS LoRa node with a Semtech SX1276 [36] as TX and a USRP N210 [37] with a UBX daughter board as RX. Both of them worked at 433MHz and were equipped with a 3.5dBi omnidirectional antenna. Unless otherwise mentioned, the default settings of LoRa were $SF = 12$, $BW = 500\text{KHz}$, $f_s = 1\text{MHz}$, and transmission power was 28dBm. We employed tags with reflective RF switch ADG902 [38] for frequency shifting, similar to the tags utilized in the work [34]. The shifting frequencies of tags ranged from 200KHz to 400KHz. We leveraged the UHD+GNU-Radio library to obtain I/Q samples and implemented LoMu in MATLAB for processing. Our implementation acquired sensing results both online and offline.

B. Benchmark Experiments

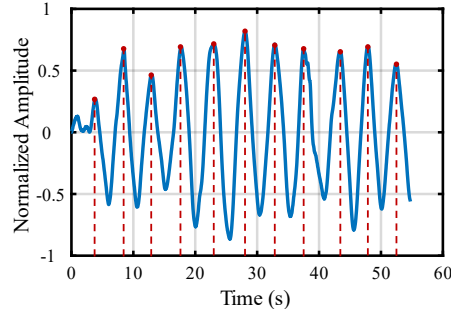
We conducted benchmark experiments on campus roads, as shown in Fig. 9. To regulate the moving amplitude and speed of tags, a slide rail was employed. Tags were placed on the slider approximately 30cm away from the COTS LoRa node, a setup similar to that used in Palantir [25]. We present the cumulative distribution function (CDF) of each experimental result.

1) *Impact of TX-RX distance:* We carried out experiments at variations TX-RX distances to access the sensing range of LoMu. Fig. 10 illustrates the CDF of tag motion frequency. The median error of LoMu increased from 0.1% marginally to 0.5% as the TX-RX distance extended from 50m to 400m. This slight increase in errors is attributed to the degradation of SNR, leading to imprecise signal extraction and more sensing errors. Notably, compared with the state-of-the-art Palantir [25], which achieved a distance of 100m, LoMu demonstrated a significant improvement, reaching a distance of 400m with as low as 0.7% average error. This enhanced sensing range is attributed to LoMu's ability to concentrate all the energy of backscatter signals.

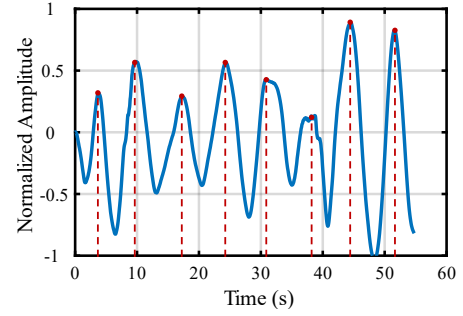
2) *Impact of Motion Amplitude and Speed:* In this experiment, we varied the moving amplitude and speed of the tag to evaluate the performance of LoMu under different motion scenarios. The ground truth was obtained from the settings of the slide rail, with a fixed distance of 150m between TX and RX. It is noteworthy that LoMu is the sole technology capable of sensing targets at this remarkable distance. Fig. 11 and Fig. 12 present the results. The median sensing error across



(a) Tag on the shirt.



(b) Sensing result of volunteer 1.



(c) Sensing result of volunteer 2.

Fig. 14: A case study of respiration sensing in two volunteers at a distance of 150m.

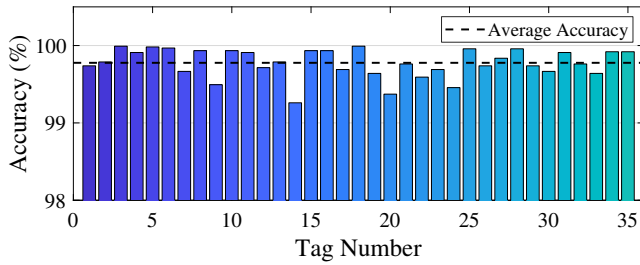


Fig. 15: Multi-tag scenario.

all settings was consistently below 0.4%, highlighting LoMu's adaptability to diverse sensing scenarios. Unlike Palantir [25], which relies on waveform peaks and may benefit from steeper amplitude changes, LoMu utilizes FFT to gather all the information within a period, ensuring effective performance across various motion patterns.

3) *Impact of Interference*: In this experiment, we categorized environmental interference into three levels to assess the robustness of LoMu. Conducted on the campus roads, the experiments involved intermittent passage of interference objects, with their numbers quantified for evaluation. The distance between TX and RX was 150m. Fig. 13 demonstrates the CDF of tag motion frequency. As anticipated, the median error increased from 0.2% to 0.6% with higher interference intensity. The 90th percentile error reached 1.2% when the count of interference objects exceeded 6. The decrease in accuracy can be attributed to the multipath effects of signals. The movement of objects around the tag alters the path lengths of reflected signals, introducing additional changes beyond those induced by tag movements and affecting sensing accuracy. It is worth mentioning that we did not rigorously control environmental interference in the aforementioned experiments, so the CDFs of those experiments resembled that of the second interference level in this experiment.

4) *Multi-Tag Scenario*: We conducted this experiment to evaluate the performance of LoMu in a multi-target scenario. Seven sets of signals were collected as the TX transmitted quadrature chirp signals with five moving tags. These tags were positioned closely and the distance between TX and RX

was 150m. The data from these seven sets were combined and processed using LoMu. Fig. 15 depicts the sensing accuracy of each tag, showing an average accuracy of 99.8%. This demonstrates the capabilities of LoMu working with multiple TXs and tags. The subtle variations among tags can be attributed to distinct reflection factors in each tag, resulting in different SNRs. It is also worth noting that the two tags employed in this experiment had shifting frequencies of 331900Hz and 333160Hz, with a frequency difference of only 1170Hz. Despite this narrow gap, LoMu accurately distinguished between them.

C. Case Study

To showcase the feasibility of long-range multi-target respiration sensing, we conducted a case study on campus roads at a distance of 150m (Fig. 9). In this case study, we attached two tags to the shirts of two volunteers to sense their respiration (Fig. 14a). Specifically, the first volunteer was instructed to breathe naturally with a period of approximately 5s, while the second volunteer was asked to take a deep breath with a period of about 7s. Fig. 14b and Fig. 14c display the respiration waveforms of two volunteers. The detected respiration period of the first volunteer was 4.86 ± 0.44 s, and for the second volunteer, it was 6.83 ± 0.51 s. These values were approximately in line with our instructions, demonstrating the multi-target respiration sensing capability of LoMu at a distance of 150m.

V. RELATED WORKS

A. LoRa Backscatter

LoRa has attracted significant attention in recent years owing to its advantages of extended communication distance and low energy consumption, aligning well with the requirements of range-limited backscatter systems. Leveraging LoRa as the excitation signal allows backscatter systems to achieve communication ranges exceeding 1km. LoRa Backscatter [39] demonstrates a communication range of 2.8km when the tag collaborates with the RF source. PLoRa [40] utilizes ambient LoRa transmissions as excitation signals and modulates them into new standard LoRa chirp signals. Aloha [41] employs OOK modulation on ambient LoRa transmissions and achieves a balance between transmission range and link throughput.

P²LoRa [34], a work closely related to LoMu, maximizes the utility of double sidebands in backscatter signals and enables concurrent communication with 101 tags. This progress motivates us to explore the feasibility of employing LoRa backscatter signals for long-range multi-target sensing.

B. LoRa-based Sensing

In addition to its applications in communication, LoRa has found utility in various domains, including localization [31], [42]–[44], soil humidity sensing [45], and so on. Several works also take advantage of the long communication range of LoRa to extend the sensing range [25], [30], [46], [47]. Zhang et al. [30] achieve a sensing range of 25m using multiple directional antennas. However, this approach relies on distinguishing stable and moving objects in reflected signals without specific target identification. Palantir [25] employs an OOK-modulated tag to extract signals reflected from a specific target, enhancing robustness to environmental interference but limiting information to the time domain. Zhang et al. [46] utilize software-based beamforming on signals received by multiple directional antennas for multi-target sensing. However, the beamforming method's resolution becomes challenging as the sensing range increases, limiting its effectiveness. In contrast, LoMu overcomes these limitations and can sense multiple targets at any reachable distance without suffering from reduced resolution.

VI. DISCUSSION

Maximum sensing speed. The issue of modulo 2π imposes a constraint on the maximum sensing speed. Due to the double sidebands combination method, the maximum sensing speed is determined by $v_{max} = \frac{c}{4\pi f_c}$, where c is the speed of light.

Motion amplitude sensing. In the sensing model of LoMu and other works [25], [30], [46], secondary reflection paths are typically overlooked. In practical scenarios, these secondary reflection paths overlap at the receiver, introducing challenges to amplitude sensing. While one approach to address this problem is to distinguish each secondary reflection path by employing a large bandwidth, this proves impractical for LoRa technology, which is inherently bandwidth-limited.

Tag Deployment. Like many other backscatter studies [25], [34], [48], it is recommended to position tags in close proximity to either TX or RX. Nevertheless, when tags are within sensing range, LoMu exhibits the capability to handle them simultaneously no matter how densely they are deployed.

Multiple transceivers. In LoMu, as long as the transmitter selects quadrature signals, multiple receivers can collaborate with multiple transmitters without interference. This opens the door to complex applications such as gesture recognition, position tracking, and trajectory reconstruction, which could be explored in future work.

VII. CONCLUSION

In this work, we present LoMu, the first long-range multi-target backscatter sensing system designed for low-cost tags under ambient LoRa. We formulate the sensing process for

tags and highlight practical challenges, such as near-far interference between multiple tags, phase offsets induced by unsynchronized transceivers, and phase errors resulting from frequency drift in low-cost tags. To address these challenges, we present the design principles of LoMu. Our extensive experimental results showcase LoMu's ability to accurately sense at least 35 tags simultaneously. With a sensing range of 400m, LoMu outperforms the state-of-the-art by $4\times$. Moreover, the average sensing error at this distance is impressively low at 0.7%. We believe the long-range multi-target sensing capabilities of LoMu will push backscatter sensing a step.

ACKNOWLEDGMENTS

This work is in part supported by National Key R&D Program of China 2022YFC3801300, National Natural Science Foundation of China (U22A2031, No. 61932013, 62172250). We thank all the anonymous reviewers for their valuable comments and helpful suggestions.

REFERENCES

- [1] L. Yang, Y. Li, Q. Lin, X.-Y. Li, and Y. Liu, "Making sense of mechanical vibration period with sub-millisecond accuracy using backscatter signals," in *Proceedings of ACM MobiCom*, 2016, pp. 16–28. I
- [2] L. Yang, Y. Li, Q. Lin, H. Jia, X.-Y. Li, and Y. Liu, "Tagbeat: Sensing mechanical vibration period with cots rfid systems," *IEEE/ACM Transactions on Networking*, vol. 25, no. 6, pp. 3823–3835, 2017. I
- [3] B. Xie, J. Xiong, X. Chen, and D. Fang, "Exploring commodity rfid for contactless sub-millimeter vibration sensing," in *Proceedings of ACM SenSys*, 2020, pp. 15–27. I, II-C, II-C
- [4] C. Duan, L. Yang, Q. Lin, Y. Liu, and L. Xie, "Robust spinning sensing with dual-rfid-tags in noisy settings," *IEEE Transactions on Mobile Computing*, vol. 18, no. 11, pp. 2647–2659, 2018. I
- [5] P. Li, Z. An, L. Yang, and P. Yang, "Towards physical-layer vibration sensing with rfids," in *Proceedings of IEEE INFOCOM*. IEEE, 2019, pp. 892–900. I
- [6] G. Wang, C. Qian, J. Han, and H. Cai, "Poster: Combating multipaths to enable rfid sensing in practical environments," in *Proceedings of ACM MobiCom*, 2017, pp. 588–590. I
- [7] B. Liang, P. Wang, R. Zhao, H. Guo, P. Zhang, J. Guo, S. Zhu, H. H. Liu, X. Zhang, and C. Xu, "Rf-chord: Towards deployable rfid localization system for logistic networks," in *Proceedings of USENIX NSDI*, 2023, pp. 1783–1799. I
- [8] E. Soltanaghaei, A. Dongare, A. Prabhakara, S. Kumar, A. Rowe, and K. Whitehouse, "Tagfi: Locating ultra-low power wifi tags using unmodified wifi infrastructure," *Proceedings of the ACM on Interactive, Mobile, Wearable and Ubiquitous Technologies*, vol. 5, no. 1, pp. 1–29, 2021. I
- [9] M. Kotaru, K. Joshi, D. Bharadia, and S. Katti, "Spotfi: Decimeter level localization using wifi," in *Proceedings of ACM SIGCOMM*, 2015, pp. 269–282. I
- [10] R. H. Venkatnarayan, G. Page, and M. Shahzad, "Multi-user gesture recognition using wifi," in *Proceedings of ACM MobiSys*, 2018, pp. 401–413. I
- [11] K. Niu, F. Zhang, Z. Chang, and D. Zhang, "A fresnel diffraction model based human respiration detection system using cots wi-fi devices," in *Proceedings of ACM UbiComp*, 2018, pp. 416–419. I
- [12] Y. Zeng, D. Wu, J. Xiong, E. Yi, R. Gao, and D. Zhang, "Farsense: Pushing the range limit of wifi-based respiration sensing with csi ratio of two antennas," *Proceedings of the ACM on Interactive, Mobile, Wearable and Ubiquitous Technologies*, vol. 3, no. 3, pp. 1–26, 2019. I
- [13] J. Hu, T. Zheng, Z. Chen, H. Wang, and J. Luo, "Muse-fi: Contactless multi-person sensing exploiting near-field wi-fi channel variation," in *Proceedings of ACM MobiCom*, 2023, pp. 1–15. I
- [14] Y. Yang, J. Cao, X. Liu, and X. Liu, "Multi-breath: Separate respiration monitoring for multiple persons with uwb radar," in *Proceedings of IEEE COMPSAC*, vol. 1. IEEE, 2019, pp. 840–849. I

- [15] S. Li, Z. Wang, F. Zhang, and B. Jin, "Fine-grained respiration monitoring during overnight sleep using ir-uwB radar," in *Proceedings of EAI MobiQuitous*. Springer, 2022, pp. 84–101. I
- [16] T. Zheng, Z. Chen, S. Zhang, C. Cai, and J. Luo, "More-fi: Motion-robust and fine-grained respiration monitoring via deep-learning uwB radar," in *Proceedings of ACM SenSys*, 2021, pp. 111–124. I
- [17] J. Yang, B. Dong, and J. Wang, "Vuloc: Accurate uwB localization for countless targets without synchronization," *Proceedings of the ACM on Interactive, Mobile, Wearable and Ubiquitous Technologies*, vol. 6, no. 3, pp. 1–25, 2022. I
- [18] A. Ahmad, J. C. Roh, D. Wang, and A. Dubey, "Vital signs monitoring of multiple people using a fmcw millimeter-wave sensor," in *Proceedings of IEEE RadarConf*. IEEE, 2018, pp. 1450–1455. I
- [19] S. M. Islam, N. Motoyama, S. Pacheco, and V. M. Lubecke, "Non-contact vital signs monitoring for multiple subjects using a millimeter wave fmcw automotive radar," in *Proceedings of IEEE/MTT-S International Microwave Symposium (IMS)*. IEEE, 2020, pp. 783–786. I
- [20] E. Turppa, J. M. Kortelainen, O. Antropov, and T. Kiuru, "Vital sign monitoring using fmcw radar in various sleeping scenarios," *Sensors*, vol. 20, no. 22, p. 6505, 2020. I
- [21] T. Li, C. An, Z. Tian, A. T. Campbell, and X. Zhou, "Human sensing using visible light communication," in *Proceedings of ACM MobiCom*, 2015, pp. 331–344. I
- [22] R. H. Venkatnarayan and M. Shahzad, "Gesture recognition using ambient light," *Proceedings of the ACM on Interactive, Mobile, Wearable and Ubiquitous Technologies*, vol. 2, no. 1, pp. 1–28, 2018. I
- [23] C. An, T. Li, Z. Tian, A. T. Campbell, and X. Zhou, "Visible light knows who you are," in *Proceedings of the 2nd International Workshop on Visible Light Communications Systems*, 2015, pp. 39–44. I
- [24] P. Xie, L. Li, J. Wang, and Y. Liu, "Litag: localization and posture estimation with passive visible light tags," in *Proceedings of the 18th Conference on Embedded Networked Sensor Systems*, 2020, pp. 123–135. I
- [25] H. Jiang, J. Zhang, X. Guo, and Y. He, "Sense me on the ride: Accurate mobile sensing over a lora backscatter channel," in *Proceedings of ACM SenSys*, 2021, pp. 125–137. I, I, II-C, II-C, III-F, IV-B, IV-B1, IV-B2, V-B, V-B, VI
- [26] S. Zhang, W. Wang, N. Zhang, and T. Jiang, "Lora backscatter assisted state estimator for micro aerial vehicles with online initialization," *IEEE Transactions on Mobile Computing*, vol. 21, no. 11, pp. 4038–4050, 2021. I, I
- [27] R. Nandakumar, V. Iyer, and S. Gollakota, "3d localization for sub-centimeter sized devices," in *Proceedings of ACM SenSys*, 2018, pp. 108–119. I
- [28] S. Zhang, W. Wang, N. Zhang, and T. Jiang, "Rf backscatter-based state estimation for micro aerial vehicles," in *Proceedings of IEEE INFOCOM*. IEEE, 2020, pp. 209–217. I
- [29] J. Xiong, K. Sundaresan, and K. Jamieson, "Tonetrack: Leveraging frequency-agile radios for time-based indoor wireless localization," in *Proceedings of ACM MobiCom*, 2015, pp. 537–549. I
- [30] F. Zhang, Z. Chang, K. Niu, J. Xiong, B. Jin, Q. Lv, and D. Zhang, "Exploring lora for long-range through-wall sensing," *Proceedings of the ACM on Interactive, Mobile, Wearable and Ubiquitous Technologies*, vol. 4, no. 2, pp. 1–27, 2020. I, II-C, II-C, V-B, V-B, VI
- [31] J. Jiang, J. Wang, Y. Chen, Y. Liu, and Y. Liu, "LocRa: Enable practical long-range backscatter localization for low-cost tags," in *Proceedings of ACM MobiSys*. ACM, 2023. I, V-B
- [32] NI, "Understanding ffts and windowing," <https://download.ni.com/evaluation/pxi/Understanding%20FFTs%20and%20Windowing.pdf>. III-C
- [33] M. Mottaghi-Kashtiban and M. Shayesteh, "New efficient window function, replacement for the hamming window," *IET Signal Processing*, vol. 5, no. 5, pp. 499–505, 2011. III-C
- [34] J. Jiang, Z. Xu, F. Dang, and J. Wang, "Long-range ambient lora backscatter with parallel decoding," in *Proceedings of ACM MobiCom*, 2021, pp. 684–696. III-D, IV-A, V-A, VI
- [35] MathWorks, "Understanding kalman filters," <https://ww2.mathworks.cn/videos/series/understanding-kalman-filters.html>. III-F
- [36] Semtech, "SX1276," <https://www.semtech.com/products/wireless-rf/lora-connect/sx1276>. IV-A
- [37] E. Research, "USRP N210," <https://www.ettus.com/all-products/un210-kit/>. IV-A
- [38] A. Devices, "ADG902," https://www.analog.com/media/en/technical-documentation/data-sheets/ADG901_902.pdf. IV-A
- [39] V. Talla, M. Hessar, B. Kellogg, A. Najafi, J. R. Smith, and S. Gollakota, "Lora backscatter: Enabling the vision of ubiquitous connectivity," *Proceedings of the ACM on Interactive, Mobile, Wearable and Ubiquitous Technologies*, vol. 1, no. 3, pp. 1–24, 2017. V-A
- [40] Y. Peng, L. Shangguan, Y. Hu, Y. Qian, X. Lin, X. Chen, D. Fang, and K. Jamieson, "Plora: A passive long-range data network from ambient lora transmissions," in *Proceedings of ACM SIGCOMM*, 2018, pp. 147–160. V-A
- [41] X. Guo, L. Shangguan, Y. He, J. Zhang, H. Jiang, A. A. Siddiqi, and Y. Liu, "Aloba: rethinking on-off keying modulation for ambient lora backscatter," in *Proceedings of ACM SenSys*, 2020, pp. 192–204. V-A
- [42] B. Islam, M. T. Islam, and S. Nirjon, "Feasibility of lora for indoor localization," *Appl. Sci*, vol. 2017, p. 8565550, 2017. V-B
- [43] C. Gu, L. Jiang, and R. Tan, "Lora-based localization: Opportunities and challenges," *arXiv preprint arXiv:1812.11481*, 2018. V-B
- [44] K.-H. Lam, C.-C. Cheung, and W.-C. Lee, "Rssi-based lora localization systems for large-scale indoor and outdoor environments," *IEEE Transactions on Vehicular Technology*, vol. 68, no. 12, pp. 11 778–11 791, 2019. V-B
- [45] Z. Chang, F. Zhang, J. Xiong, J. Ma, B. Jin, and D. Zhang, "Sensor-free soil moisture sensing using lora signals," *Proceedings of the ACM on Interactive, Mobile, Wearable and Ubiquitous Technologies*, vol. 6, no. 2, pp. 1–27, 2022. V-B
- [46] F. Zhang, Z. Chang, J. Xiong, R. Zheng, J. Ma, K. Niu, B. Jin, and D. Zhang, "Unlocking the beamforming potential of lora for long-range multi-target respiration sensing," *Proceedings of the ACM on Interactive, Mobile, Wearable and Ubiquitous Technologies*, vol. 5, no. 2, pp. 1–25, 2021. V-B, V-B, VI
- [47] Z. Song, S. Tong, and J. Wang, "Losense: Integrated long-range sensing and communication with lora signals," in *2023 IEEE 31st International Conference on Network Protocols (ICNP)*. IEEE, 2023, pp. 1–11. V-B
- [48] A. Varshney, O. Harms, C. Pérez-Penichet, C. Rohner, F. Hermans, and T. Voigt, "Lorea: A backscatter architecture that achieves a long communication range," in *Proceedings of ACM SenSys*, 2017, pp. 1–14. VI